Astronomy & Astrophysics

Detection of He I λ10830 Å absorption on HD 189733 b with CARMENES high-resolution transmission spectroscopy

M. Salz[1], S. Czesla[1], P. C. Schneider[1], E. Nagel[1], J. H. M. M. Schmitt[1], L. Nortmann[2,3], F. J. Alonso-Floriano[4], M. López-Puertas[5], M. Lampón[5], F. F. Bauer[5,6], I. A. G. Snellen[4], E. Pallé[2,3], J. A. Caballero[7], F. Yan[8], G. Chen[2,3,9], J. Sanz-Forcada[7], P. J. Amado[5], A. Quirrenbach[10], I. Ribas[11,12], A. Reiners[6], V. J. S. Béjar[2,3], N. Casasayas-Barris[2,3], M. Cortés-Contreras[7], S. Dreizler[6], E. W. Guenther[13], T. Henning[8], S. V. Jeffers[6], A. Kaminski[10], M. Kürster[8], M. Lafarga[11], L. M. Lara[5], K. Molaverdikhani[8], D. Montes[14], J. C. Morales[11], A. Sánchez-López[5], W. Seifert[10], M. R. Zapatero Osorio[15], and M. Zechmeister[6]

[1] Hamburger Sternwarte, Universität Hamburg, Gojenbergsweg 112, 21029 Hamburg, Germany
e-mail: msalz@hs.uni-hamburg.de
[2] Instituto de Astrofísica de Canarias, Vía Láctea s/n, 38205 La Laguna, Tenerife, Spain
[3] Departamento de Astrofísica, Universidad de La Laguna, 38206 La Laguna, Tenerife, Spain
[4] Leiden Observatory, Leiden University, Postbus 9513, 2300 RA, Leiden, The Netherlands
[5] Instituto de Astrofísica de Andalucía (IAA-CSIC), Glorieta de la Astronomía s/n, 18008 Granada, Spain
[6] Institut für Astrophysik, Georg-August-Universität, Friedrich-Hund-Platz 1, 37077 Göttingen, Germany
[7] Centro de Astrobiología, CSIC-INTA, ESAC Campus, Camino bajo del castillo s/n, 28692 Villanueva de la Cañada, Madrid, Spain
[8] Max-Planck-Institut für Astronomie, Königstuhl 17, 69117 Heidelberg, Germany
[9] Key Laboratory of Planetary Sciences, Purple Mountain Observatory, Chinese Academy of Sciences, Nanjing 210008, PR China
[10] Landessternwarte, Zentrum für Astronomie der Universität Heidelberg, Königstuhl 12, 69117 Heidelberg, Germany
[11] Institut de Ciències de l'Espai (ICE, CSIC), Campus UAB, C/ de Can Magrans s/n, 08193 Cerdanyola del Vallès, Spain
[12] Institut d'Estudis Espacials de Catalunya (IEEC), 08034 Barcelona, Spain
[13] Thüringer Landessternwarte Tautenburg, Sternwarte 5, 07778 Tautenburg, Germany
[14] Departamento de Astrofísica y Ciencias de la Atmósfera, Facultad de Ciencias Físicas, Universidad Complutense de Madrid, 28040 Madrid, Spain
[15] Centro de Astrobiología, CSIC-INTA, Carretera de Ajalvir km 4, 28850 Torrejón de Ardoz, Madrid, Spain

ABSTRACT

We present three transit observations of HD 189733 b obtained with the high-resolution spectrograph CARMENES at Calar Alto. A strong absorption signal is detected in the near-infrared He I triplet at 10830 Å in all three transits. During mid-transit, the mean absorption level is $0.88 \pm 0.04\%$ measured in a ± 10 km s^{-1} range at a net blueshift of -3.5 ± 0.4 km s^{-1} (10829.84–10830.57 Å). The absorption signal exhibits radial velocities of $+6.5 \pm 3.1$ km s^{-1} and -12.6 ± 1.0 km s^{-1} during ingress and egress, respectively; all radial velocities are measured in the planetary rest frame. We show that stellar activity related pseudo-signals interfere with the planetary atmospheric absorption signal. They could contribute as much as 80% of the observed signal and might also affect the observed radial velocity signature, but pseudo-signals are very unlikely to explain the entire signal. The observed line ratio between the two unresolved and the third line of the He I triplet is 2.8 ± 0.2, which strongly deviates from the value expected for an optically thin atmospheres. When interpreted in terms of absorption in the planetary atmosphere, this favors a compact helium atmosphere with an extent of only 0.2 planetary radii and a substantial column density on the order of 4×10^{12} cm^{-2}. The observed radial velocities can be understood either in terms of atmospheric circulation with equatorial superrotation or as a sign of an asymmetric atmospheric component of evaporating material. We detect no clear signature of ongoing evaporation, like pre- or post-transit absorption, which could indicate material beyond the planetary Roche lobe, or radial velocities in excess of the escape velocity. These findings do not contradict planetary evaporation, but only show that the detected helium absorption in HD 189733 b does not trace the atmospheric layers that show pronounced escape signatures.

Key words. planets and satellites: atmospheres – planets and satellites: individual: HD 189773 b – planet-star interactions – techniques: spectroscopic – infrared: planetary systems – stars: activity

1. Introduction

The atmospheres of close-in planets are exposed to intense high-energy irradiation by their host stars. Stellar extreme-UV and X-ray photons deposit large amounts of energy high up in the planetary atmosphere, capable of powering planetary evaporation with supersonic wind speeds of around 10 km s^{-1} (e.g., Watson et al. 1981; Lammer et al. 2003; Salz et al.

2016). Such radiation-induced planetary mass loss may be strong enough to completely evaporate the gaseous envelopes of small planets (Lecavelier des Etangs et al. 2004), which would explain the detected population of hot super-Earths (Lundkvist et al. 2016; Fulton et al. 2017).

An extended hydrogen atmosphere around KELT-9 b was recently detected via optical Hα transit spectroscopy with

CARMENES (Yan & Henning 2018). To date, the strongest observational evidence for the existence of planetary evaporation winds comes from Lyα and UV transit spectroscopy. Prominent examples are the planets HD 209458 b, HD 189733 b, WASP-12 b, and GJ 436 b (Vidal-Madjar et al. 2003, 2004, 2008, 2013; Ehrenreich et al. 2008, 2015; Ben-Jaffel & Sona Hosseini 2010; Linsky et al. 2010; Lecavelier des Etangs et al. 2010, 2012; Fossati et al. 2010; Haswell et al. 2012; Bourrier et al. 2013; Ben-Jaffel & Ballester 2013; Kulow et al. 2014; Ballester & Ben-Jaffel 2015; Lavie et al. 2017). Lyα observations can only be obtained using space-borne instrumentation and, more importantly, interstellar material absorbs the Lyα line core even for the nearest stars. This absorption suppresses any signal at velocities of around 10 km s⁻¹, which is the characteristic speed of supersonic evaporation close to the planet. Therefore, alternative diagnostics for planetary winds are highly desirable.

Seager & Sasselov (2000) were the first to emphasize the potential of the He I λ10830 Å triplet lines to study upper atmospheric layers, which are the launching region of the planetary wind. The triplet is composed of two closely spaced lines with central wavelengths[1] of 10830.33 and 10830.25 Å and a third weaker line at 10829.09 Å. These lines are accessible from the ground and are not affected by interstellar absorption. For example, along one line of sight, Indriolo et al. (2009) derived an upper limit of 3.2×10^9 cm⁻² for the interstellar He I triplet state column density, which is two to three orders of magnitude lower than the column densities derived in the following. Recently, Oklopčić & Hirata (2018) used 1D models of the escaping atmospheres of GJ 436 b and HD 209458 b, including all sources and sinks of the triplet ground state, and showed that planetary absorption in the He I λ10830 Å lines could reach several percent.

Absorption in the He I triplet lines in the stellar atmosphere is related to stellar activity features (e.g., Zarro & Zirin 1986; Sanz-Forcada & Dupree 2008), which can cause serious complications for exoplanet transit observations. In the solar context, the lines have been studied in detail by Avrett et al. (1994) and Mauas et al. (2005). The Sun shows a highly inhomogeneous surface distribution of He I λ10830 Å absorption (see Fig. 1 of Andretta et al. 2017), with absorption practically restricted to active regions (Avrett et al. 1994). Accordingly, the disk-integrated absorption reveals 10% rotational variation and 30% variation over activity cycles (Harvey & Livingston 1994).

While a search with the VLT/ISAAC instrument for atmospheric He I λ10830 Å absorption of the hot Jupiter orbiting the inactive host star HD 209458 resulted in an upper limit of 0.5% in a 3 Å wide window (Moutou et al. 2003), the signal has now been detected in WASP-107 b with Wide Field Camera 3 on board the *Hubble* Space Telescope. Here, 0.05% excess absorption was observed over a 98 Å wide window (Spake et al. 2018). In Nortmann et al. (2018), we report 3.6 ± 0.2% He I absorption observed during the transit of WASP-69 b at high spectral resolution with the CARMENES spectrograph. Here, we present the detection and analysis of He I absorption in the HD 189733 system.

2. The HD 189733 exoplanetary system

The hot Jupiter HD 189733 b is among the best-studied planets to date. The 1.16 $M_{\rm jup}$ mass planet orbits an active K dwarf with a period of 2.2 days (Bouchy et al. 2005); see

---

[1] We use air wavelengths throughout the manuscript.

Table 1. Adopted system parameters of HD 189733.

Parameter	Value	Reference
α [J2015.5]	20:00:43.70	*Gaia* DR2[a]
δ [J2015.5]	+22:42:35.3	*Gaia* DR2[a]
d	19.775 ± 0.013 pc	*Gaia* DR2[a]
$R_{\rm S}$[b]	0.805 (16) $R_\odot$	Boyajian et al. (2015)
$M_{\rm S}$	$0.846^{+0.06}_{-0.049}$ $M_\odot$	de Kok et al. (2013)
$P_{\rm rot}$	11.953 (9) d	Henry & Winn (2008)
$K_{\rm S}$	$201.96^{+1.07}_{-0.63}$ m s⁻¹	Triaud et al. (2009)
$v_{\rm sys}$	-2.361 (3) km s⁻¹	Bouchy et al. (2005)
T_0 [BJD$_{\rm TDB}$]	2453955.5255511 (88)	Baluev et al. (2015)
$P_{\rm orb}$	2.218575200 (77) d	Baluev et al. (2015)
b[c]	0.6636 (19)	Baluev et al. (2015)
$R_{\rm p}/R_{\rm s}$	0.15712 (40)	Baluev et al. (2015)
$M_{\rm p}$	$1.162^{+0.058}_{-0.039}$ $M_{\rm jup}$	de Kok et al. (2013)
$a/R_{\rm s}$	8.863 (20)	Agol et al. (2010)
i	85.710 (24)°	Agol et al. (2010)
$K_{\rm p}$	162.2 (3.3) km s⁻¹	This work[d]

Notes. [a]Gaia Collaboration (2016); Brown et al. (2018). [b]Measured by interferometry. The stellar radius determines the absolute dimension of the semimajor axis and the planetary radial velocity half amplitude $K_{\rm p}$. [c]Impact parameter. [d]$K_{\rm p} = 2\pi a/P_{\rm orb} \sin i$.

Table 1 for details. Its atmospheric transmission is likely dominated by Rayleigh scattering in the wavelength range from 3000 to 10 000 Å (Pont et al. 2008, 2013; Lecavelier Des Etangs et al. 2008; Sing et al. 2009, 2011, 2016; Gibson et al. 2012). However, the contribution of unocculted stellar spots to the alleged Rayleigh scattering slope remains uncertain (McCullough et al. 2014). In lower atmospheric layers, absorption of carbon monoxide (de Kok et al. 2013; Rodler et al. 2013; Brogi et al. 2016) and water (Birkby et al. 2013; McCullough et al. 2014; Brogi et al. 2018) has been detected. Measurements of sodium absorption were used to reconstruct the atmospheric temperature-pressure profile up to the lower thermosphere (Redfield et al. 2008; Huitson et al. 2012; Wyttenbach et al. 2015; Louden & Wheatley 2015; Khalafinejad et al. 2017). A reported detection of planetary Hα absorption by Jensen et al. (2012) remains difficult to interpret due to the confounding spectral effects of stellar variability (Barnes et al. 2016; Cauley et al. 2017).

HD 189733 is an active star with strong emission cores in the Ca II H&K lines, resulting in a high value of 0.508 for the Mount Wilson S-index (Baliunas et al. 1995; Knutson et al. 2010). The star shows frequent flaring at optical and X-ray wavelengths (Pillitteri et al. 2014; Klocová et al. 2017) and an overall X-ray luminosity of $\approx 2 \times 10^{28}$ erg s⁻¹ (Hünsch et al. 1999), which places it in the top decile of the X-ray luminosity distribution function (Schmitt et al. 1995). Sanz-Forcada et al. (2011) reconstructed an extreme UV luminosity of 3×10^{28} erg s⁻¹, which implies substantial high-energy irradiation levels on HD 189733 b that ought to trigger an evaporative wind in the upper planetary atmosphere (Salz et al. 2016). The escape of this upper atmosphere has been detected through hydrogen Lyα and oxygen absorption (Lecavelier des Etangs et al. 2010, 2012; Bourrier et al. 2013; Ben-Jaffel & Ballester 2013), and Poppenhaeger et al. (2013) proposed a tentative 6–8% deep X-ray transit. These findings make HD 189733 b a promising candidate to search for He I λ10830 Å absorption.

Table 2. Observing details.

Night	Date	Proposal ID	Principal investigator	Calar Alto Archive ID	No. of spectra[a]	S/N[b] at 10830 Å	Pre-/post-transit (h)	Mid-transit time (BJD TDB)
1	2016-08-08	H16-3.5-024	P. J. Amado	246903-246952	45 (1/1)	160	1.0 / 1.0	2457609.51891
2	2016-09-17	H16-3.5-024	P. J. Amado	249745-249798	50 (4/2)	210	2.3 / 1.2	2457649.45326
3	2017-09-07	H16-3.5-022	J. A. Caballero	263103-263156	46 (1/1)	240	1.7 / 1.0	2458004.42529

Notes. [a]Number of spectra neglected at the beginning and end of the night in parentheses. [b]One divided by the nightly average standard deviation of the residual spectra in the continuum surrounding the He I λ10830 Å lines.

3. Observations and data analysis

We analyzed three spectral transit time series[2] of HD 189733 taken on 8 Aug 2016, 17 Sept 2016, and 7 Sept 2017, in the following referred to as night 1, 2, and 3. The observations were taken with the CARMENES spectrograph, mounted at the 3.5 m telescope at the Calar Alto Observatory; see Quirrenbach et al. (2016) for a detailed description. The CARMENES spectrographs simultaneously cover the visual and near-infrared (NIR) ranges (5500–9600 Å and 9600–17 200 Å) with a nominal resolution of 94 600 and 80 400, respectively, and a sampling of 2.3 pixel per resolution element around the He I triplet. The two independent channels are housed in vacuum tanks to optimize radial velocity precision. The NIR spectrograph is fed by two fibers. In our configuration, fiber A carried the light from the target and fiber B was used to obtain simultaneous sky spectra. The data reduction was carried out with the pipeline (CARACAL v2.10; Caballero et al. 2016).

The exposure time of our spectra was 198 s throughout the campaign. Further details on the observations and the observing conditions are provided in Table 2 and Fig. 1. The airmass was mostly below 1.5 and the typical seeing was better than 1″. During night 3 the column of water vapor was higher, but this night offered the best seeing conditions and resulted in the highest signal-to-noise ratio (S/N) per spectrum. The S/N during the first two nights may have been affected by stability issues with the NIR channel, which is evident in the NIR radial velocity measurements (see Appendix C).

Scrutinizing the spectral time series, we identified a total of four spectral regions that exhibited excessive spectral variations in all three nights. These spectral anomalies were likely caused by bad detector pixels and were, therefore, discarded in our analysis. Fortunately, none of the affected regions overlapped with the He I lines (shaded regions in Fig. 2).

3.1. Telluric correction

Although the line cores of the He I λ10830 Å lines are not blended with telluric lines, the spectral region is contaminated with water vapor absorption originating from the Earth's atmosphere. We used the `molecfit` software in version 1.2.0 (Smette et al. 2015; Kausch et al. 2015) to remove the telluric contribution from each individual CARMENES spectrum. A nightly mid-latitude (45°) reference model atmosphere[3] and the Global Data Assimilation System (GDAS) profiles for the location of the Calar Alto Observatory were used to create atmospheric temperature-pressure profiles for the three nights, which are
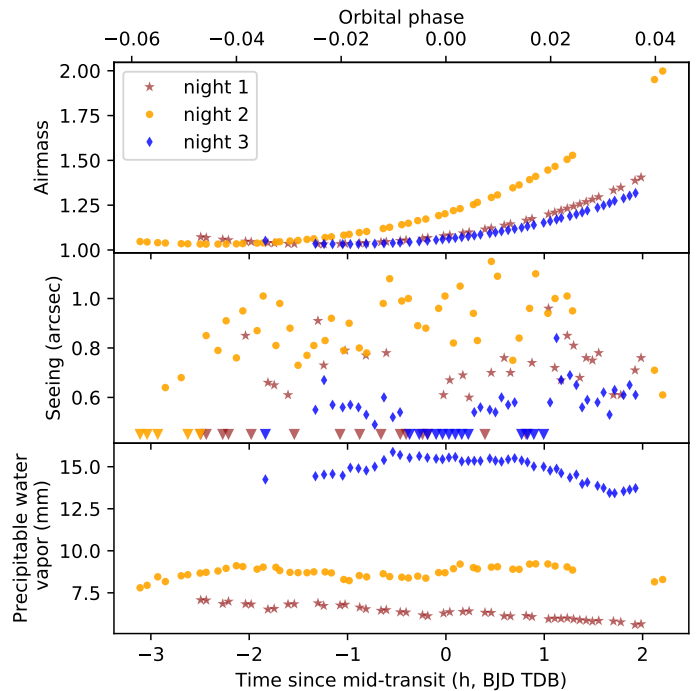
Fig. 1. Airmass, seeing, and column of precipitable water vapor during the observations. Unresolved seeing is indicated by triangles. The error bars for the water column, which was derived in the telluric correction, are smaller than the marker size.

required for the line-by-line radiative transfer in `molecfit`. We included O_2, CO_2, and CH_4 in our transmission model with fixed abundances, taken from the reference atmosphere, and fitted the precipitable water vapor.

As reported by Allart et al. (2017), the choice of the optimization ranges is crucial to derive precise transmission models with `molecfit`. We selected nine 50–100 Å broad wavelength intervals evenly distributed over the CARMENES NIR channel, taking full advantage of the large amount of telluric lines contained in this spectral region. These intervals exhibit few stellar lines, a well determined continuum level, and comprise various deep but unsaturated telluric absorption lines. Stellar features were identified and masked using a high-resolution synthetic stellar spectrum (PHOENIX; Husser et al. 2013) with $T_{eff} = 4700$ K, $\log g = 4.5$ dex, and solar metallicity. In addition, we excluded wavelength ranges with sky emission features. The instrumental line spread function was determined using hollow cathode lamp spectra. Based on the best-fit parameters derived by `molecfit`, we finally generated a transmission model for the entire wavelength range of CARMENES and corrected each science spectrum.

Telluric emission lines were removed using the sky spectrum from fiber B. We fitted and subtracted the continuum in the sky spectra and subtracted the remaining emission line spectrum from the science spectrum. The comparison of Figs. 2 and A.2 shows that the strongest emission line in the red wing of the He I triplet at 10830.91 Å was successfully removed to within the noise level. At any rate, this line can only affect the egress phase, where its position partially overlaps with the He I λ10830 Å lines. Two further telluric emission lines at 10829.01 and 10828.73 Å are located such that they could affect the analysis of the weaker triplet component at 10829 Å. However, these lines are a factor of 11 weaker than the line at 10830.91 Å. As we found no significant differences in our results when correcting or masking them, we consider these lines irrelevant.

### 3.2. Continuum normalization and stellar rest frame alignment

The continuum was normalized with a third-order polynomial and the spectra were shifted into the stellar rest frame by correcting for a systematic radial velocity of -2.361 km s^{-1} (Bouchy et al. 2005), Earth's barycentric velocity, and the stellar orbital motion. The barycentric velocity correction was computed using the `helcorr` routine[4], and mid-exposure time stamps were converted into barycentric Julian dates (BJD) in barycentric dynamic time (TDB) using the `Astropy` time package (Astropy Collaboration 2013).

For each night, the spectral alignment was controlled using the seven strongest and isolated stellar lines in the vicinity of the He I triplet (see Fig. A.1): Mg I λ10811.084 Å, Fe I λ10818.276 Å, Si I λ10827.091 Å, Ca I λ10838.970 Å, Si I λ10843.854 Å, Fe I λ10849.467 Å, and Fe I λ10863.520 Å. We found an average redshift of 360 m s^{-1} with respect to the radial velocity of Bouchy et al. (2005), which was corrected. During night 2, the instrument showed an apparent drift of $\approx$200 m s^{-1}. This drift was modeled for the out-of-transit phases with a second-order polynomial, which was then used to correct the alignment of all spectra during this night. Radial velocity drifts or offsets can occur because our observations were not obtained with a setup optimized for radial velocity measurements, i.e., the instrumental radial velocity drift was not monitored through the Fabry–Pérot in the calibration fiber. In the end, we found all seven stellar lines within $\approx$200 m s^{-1} of their nominal central wavelengths and interpolated all spectra onto a common wavelength grid.

3.3. Residual spectra

For each night, we combined the out-of-transit spectra to construct a master reference spectrum, discarding the first and last few spectra during each night for technical reasons (see Table 2). All spectra were then divided by this master out-of-transit spectrum to obtain a time series of residual spectra (see Fig. 2). In all three observed transits, a pronounced absorption feature attributable to the He I λ10830 Å lines is detected. These results are independent of our telluric emission correction (see Fig. A.2). The highest S/N was reached on night 3, during which the radial velocity of the absorption signals clearly shifts along with the orbital radial velocity of the planet in the mid-transit phase. This indicates that the absorption is indeed associated with the hot Jupiter. The association is less clear on the first

---

[4] Implemented in PyAstronomy https://github.com/sczesla/PyAstronomy and adapted from the REDUCE package (Piskunov & Valenti 2002).
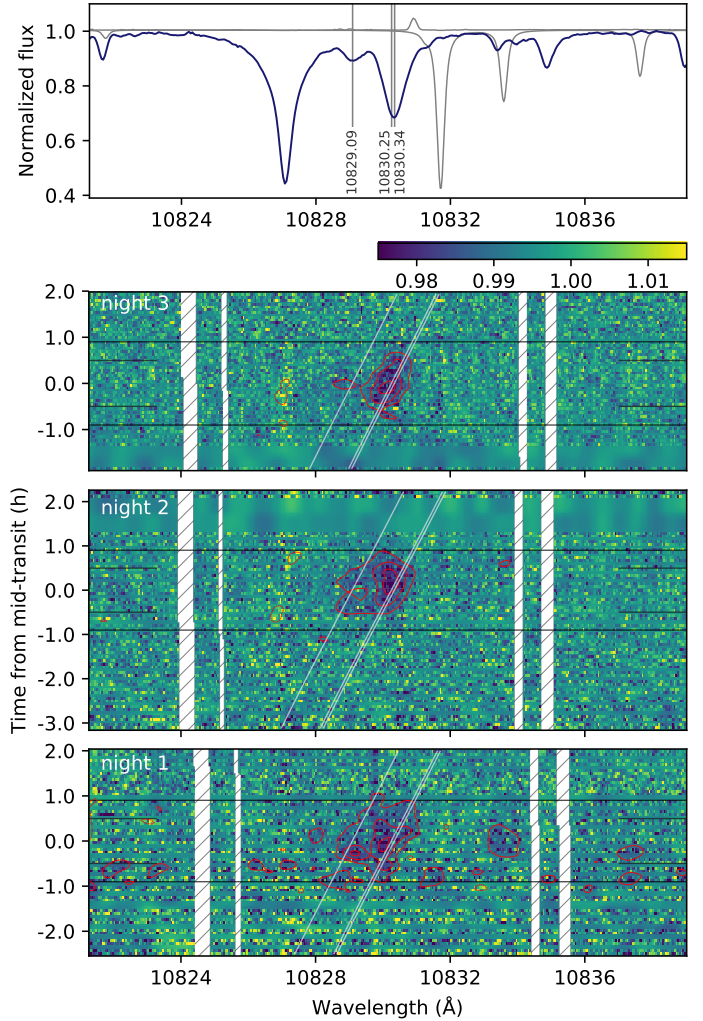
Fig. 2. *Top panel:* out-of-transit spectrum around the He I λ10830 Å lines after removal of telluric lines and averaged over the three observing nights. The triplet line positions are marked by vertical lines labeled by their central wavelength. A telluric absorption spectrum and the average telluric emission spectrum from night 3 are depicted by gray lines. *Lower panels:* time series of residual spectra for three transits of HD 189733 b in the stellar rest frame. Rows depict individual residual spectra with color-coded intensity; time progresses along the y-axis, and row height and gaps correspond to the exposure times. We use a linear interpolation over the gaps and apply a Gaussian smoothing and transparency for distinction. Masked regions are likely affected by bad pixels. First and fourth contacts of the optical transit are marked by horizontal lines, and second and third contacts are indicated by shorter vertical lines at the figure edges. The slanted lines show the position of the He I triplet lines in the planetary rest frame. Red solid and dashed contours are respectively 0.33% negative and positive variations from mean.

two nights. This is could be caused by the reduced instrumental stability and S/N (see Appendix C), but could also be related to stellar pseudo-signals interfering with the planetary He I λ10830 Å absorption signals. This possibility is further investigated in Sect. 4.1. The Rossiter–McLaughlin effect (RME) in the He I λ10830 Å lines is also superimposed on the residual spectra, but we calculate its amplitude to be smaller than 0.07%, which is negligible during the mid-transit phase (see Sect. 4.1).

The out-of-transit stellar He I λ10830 Å lines do not show detectable variation across the three observing nights or within any of them (see Fig. 2). The cores of the Ca II infrared triplet
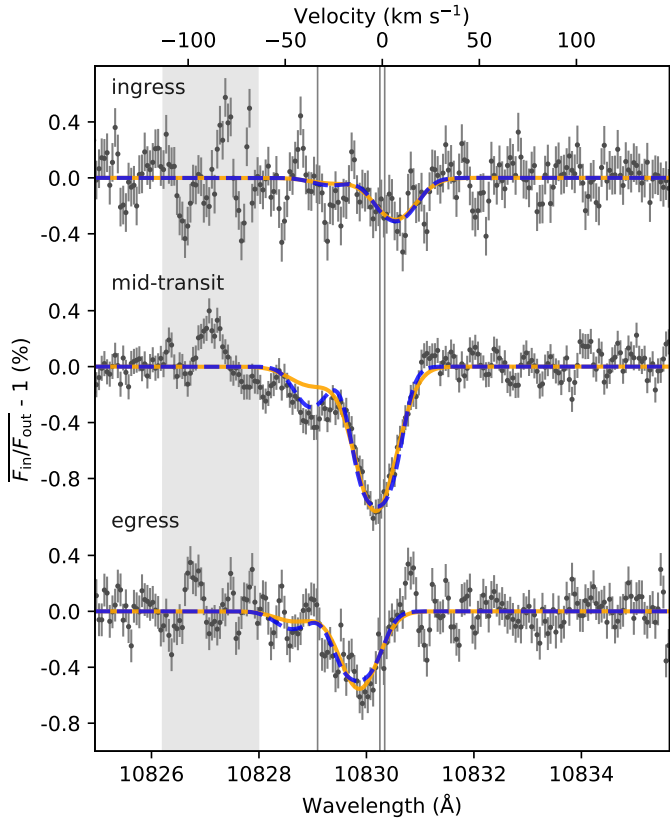
Fig. 3. Weighted mean transmission spectrum of the three observed transits split into ingress, mid-transit, and egress. The wavelengths of the triplet lines are marked by vertical lines. Compact and extended atmosphere models are depicted for each phase by blue dashed and orange solid lines, respectively (see main text). The gray shaded region was masked during the MCMC runs due to residuals in a Si I line.

lines, which are well-known activity indicators, show an activity trend during night 1 along with small activity fluctuations, but no clear signature of flaring (see Appendix B). Figure 2 exhibits a weaker feature associated with the Si I line at 10827.1 Å that exhibits a radial velocity of only about 100 m s^{-1} in the stellar rest frame. This feature can be nicely described by center-to-limb variations in combination with the RME in the stellar line (Czesla et al. 2015). There is also a slight activity trend in this line that correlates with the trend seen in the Ca II infrared triplet lines.

Using the ephemeris of Baluev et al. (2015), we shifted the residual spectra into the planetary rest frame and computed nightly means for the ingress, mid-transit, and egress phases. Observations that start after the first contact and have a mid-exposure time before the second contact were included in the ingress phase. An equivalent procedure was used for the egress phase. In total, we have 10 spectra during the ingress, 34 during mid-transit, and 13 during the egress phases. Because of the different data quality, the three nightly means were combined weighting them by the inverse variance in the surrounding continuum. The obtained mean transmission spectra are displayed in Fig. 3, and the nightly residual spectra and their variation with respect to the mean transmission spectrum are shown in Fig. A.3.

3.4. Bootstrap analysis of the absorption depth

For each phase, the mean absorption depth was calculated in a ±10 km s^{-1} window centered on the shifted signal position
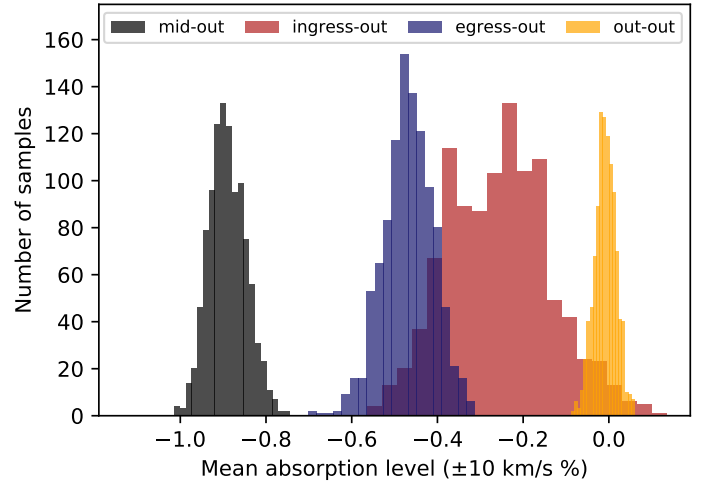
Fig. 4. Histograms of the absorption levels in the mean residual spectra for the three in-transit phases and a control out-of-transit phase during our bootstrap analysis.

determined by our model fitting in Sect. 4.2: +6.5 km s^{-1} for ingress, −3.5 km s^{-1} for mid-transit, and −12.6 km s^{-1} for egress. Errors were determined by a bootstrap method. On average, we randomly drew half of the spectra from each phase, computed the mean absorption spectrum, and determined the average absorption level. This was performed 1000 times and the resulting histograms are shown in Fig. 4. We find average absorption levels of 0.24 ± 0.12% for the ingress phase, 0.88 ± 0.04% for the mid-transit phase, and 0.46 ± 0.06% for the egress phase. We also randomly drew half of the out-of-transit residual spectra, averaged in the center of the two strong helium lines at 10830 Å in the stellar rest frame, and find zero absorption in this control sample.

The ingress signal is formally only a 2σ result and exhibits the largest scatter of the three transit phases. This cannot be caused by residual telluric contamination since the ingress signal does not overlap with any telluric emission or absorption line.

In the line core of the strong He I triplet component, the absorption depth reaches its maximum of 1.04 ± 0.09%, using the standard deviation of the surrounding continuum as error estimate. If this absorption feature is caused by the planet, its atmosphere must exhibit a radial extent of at least 0.2 R_p. The absorption signal has a total equivalent width of 12.7 ± 0.6 mÅ and we further derive a ratio of the He I λ10830 Å to λ10829 Å triplet components of 2.8 ± 0.2 by fitting Gaussians with free relative strengths. Here the errors are propagated from the bootstrap analysis.

To investigate nightly variability in the absorption depth, we repeated the bootstrap analysis for the mid-transit signals of the individual nights averaging over the full signal (−70 to +30 km s^{-1}). We measure absorption levels of 0.41 ± 0.04%, 0.39 ± 0.04%, and 0.35 ± 0.04% for nights 1, 2, and 3, respectively. While the nightly mean transmission spectra suggest some variation at different epochs (see Fig. A.3), they do not exceed the rednoise level.

3.5. Temporal evolution of the He I signal

We computed light curves of the He I signal by averaging over a broad velocity range from −20 to +15 km s^{-1} in the planetary rest frame, corresponding to 10829.57 to 10830.84 Å. This
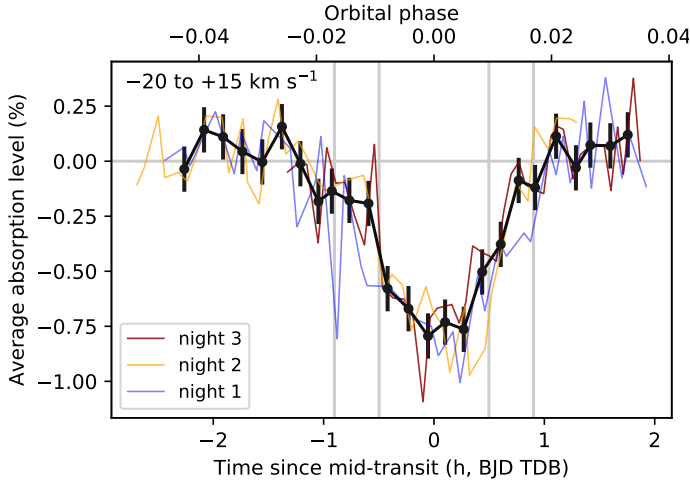
Fig. 5. Time evolution of the He I λ10830 Å signal during the three nights. Vertical lines mark the contact points of the broad band optical transit (T_1–T_4). The mean transit light curve (black line) is shown with error bars.

range covers the observed velocity shifts at ingress and egress. The light curves are depicted in Fig. 5. A light curve centered on the weak triplet component is provided in Fig. A.3. We detect no significant inter-night variations. While some apparent in-transit outliers could be associated with spot crossing events, we consider the evidence immaterial. A mean light curve was constructed by binning the three phased light curves with a temporal resolution of 10 min. The nightly weights were maintained in this procedure. Errors are obtained from the variation in the out-of-transit phase. The resulting time series is nearly symmetric with respect to the transit center. Some pre-transit absorption may be present, but the evidence remains inconclusive; we find no evidence for post-transit absorption.

4. Discussion

Our data show a clear in-transit signal in the He I triplet lines, consistently present in all three spectral transit time series. However, this signal is not necessarily caused only through absorption in a planetary atmosphere because the transit of the opaque planetary disk across an inhomogeneous stellar surface can produce pseudo-absorption and pseudo-emission signals. As a first step toward a better understanding of the presented signal, we study the two extreme cases: a heterogeneous stellar surface and no planetary He I absorption, and only planetary absorption.

4.1. Impact of a spotted stellar surface

Even without atmosphere, the transit of the planetary disk over stellar surface regions with below-average He I absorption (bright stellar surface patches) produces an apparent absorption signal in the residual spectra (pseudo-absorption). Similarly, pseudo-emission is produced when the planet traverses dark stellar surface regions with strong stellar He I absorption.

The impact of these pseudo-signals can be investigated considering the limiting scenarios. When the planet transits stellar surface patches completely lacking the He I absorption line, the maximum amount of pseudo-absorption is observed. While the amplitude of this signal only depends on the average stellar He I λ10830 Å spectrum and the optical transit depth, it is necessary

to specify the stellar He I spectrum in the eclipsed section of the disk to compute the expected pseudo-emission signal. To that end, we applied a two-component disk model, consisting only of regions that are either entirely free of absorption or show strong He I absorption.

#### 4.1.1. Filling factor of dark He I patches

An approximation of the filling factor of dark He I patches can be determined through the equivalent width (EW) ratio of the He I λ10830 Å lines and the optical He I λ5876 Å line (Andretta et al. 2017). To measure these lines, we combined all out-of-transit spectra from all nights to obtain a master spectrum. The helium He I λ10830 Å lines are located in the wing of the Si I line at 10827.091 Å (see Fig. 6). As noted by Andretta et al. (2017), this line is poorly reproduced with a single Voigt profile, so we fitted the line with two superposed Voigt profiles with the same central wavelength. The He I λ10830 Å lines were fitted with Gaussians with fixed relative wavelength but free relative strengths. The Si I line is found within the stellar rest frame velocity to an accuracy of 140 m s^{-1}, but for the He I λ10830 Å lines we find a redshift of 0.94 km s^{-1}. The main component has an equivalent width of 323 mÅ and the minor component of 52 mÅ, resulting in an EW ratio of 6.2. For the optical He I λ5876 Å line, we also fitted a Gaussian profile and derived an equivalent width of 21.5 mÅ along with a redshift of 1.3 km s^{-1}. In the fit, we neglected some minor line blends identified by Andretta et al. (2017). The resulting radial velocity shift is similar in the optical and infrared helium lines.

According to the EWs of the helium lines, HD 189733 is located above the theoretical curve for a helium spot filling factor of 100% adopted by Andretta et al. (2017, see their Fig. 10), which can likely be attributed to insufficient stellar atmosphere models. Among the stellar sample studied by Andretta et al. (2017), ε Eri shows properties comparable to HD 189733. In particular, this active K dwarf shows values of 258 and 51 mÅ for the EWs of the stellar infrared triplet components and 18.1 mÅ for the optical line along with an X-ray luminosity of 2.1×10^{28} erg s^{-1}. For ε Eri, Andretta et al. (2017) derived a minimum filling factor of 59% for dark He I patches. By analogy, we adopt a high helium spot filling factor of 75% for our pseudo-signal analysis in HD 189733. Such a large filling factor is also consistent with other aspects of our data, viz., the absence of both significant inter-transit variability in the stellar He I line and detectable spot crossing events in our data (Sects. 3.4 and 3.5).

We reconstructed the average stellar spectrum shown in the top panel of Fig. 2 by assuming that the complete stellar He I λ10830 Å absorption EW is produced by 75% dark patches on the stellar surface. For the remaining 25% of bright regions we assumed negligible He I absorption. This procedure provides estimates for the spectra of bright and dark patches on the stellar surface.

4.1.2. Quantifying the pseudo-signal

To compute model spectral time series, we adopted a discretized stellar surface, rigidly rotating with a projected rotation velocity, $v \sin i$, of 3.5 km s^{-1}. In the planetary rest frame, the stellar surface is Doppler shifted, most pronouncedly during ingress and egress. The amount of this shift depends on the relative motion of the star and the planet and the motion of the rotating stellar surface elements. We used the two-component stellar surface
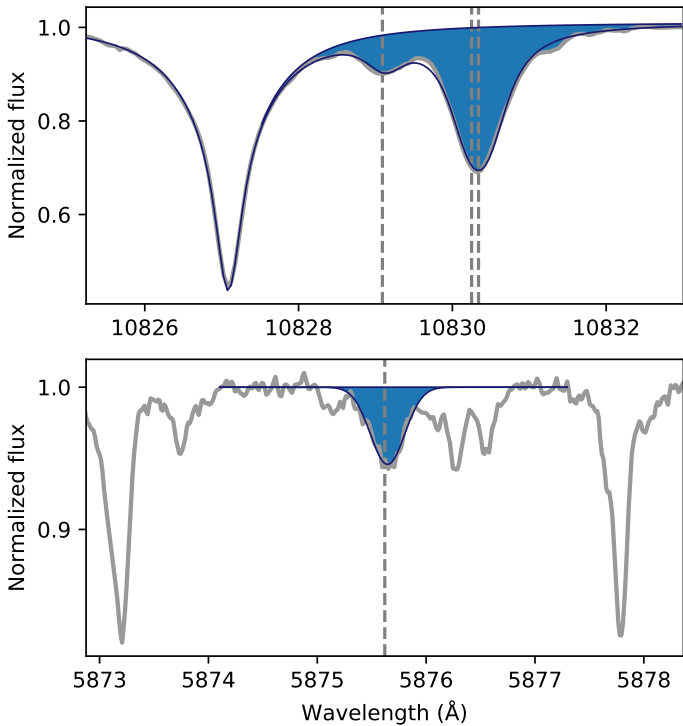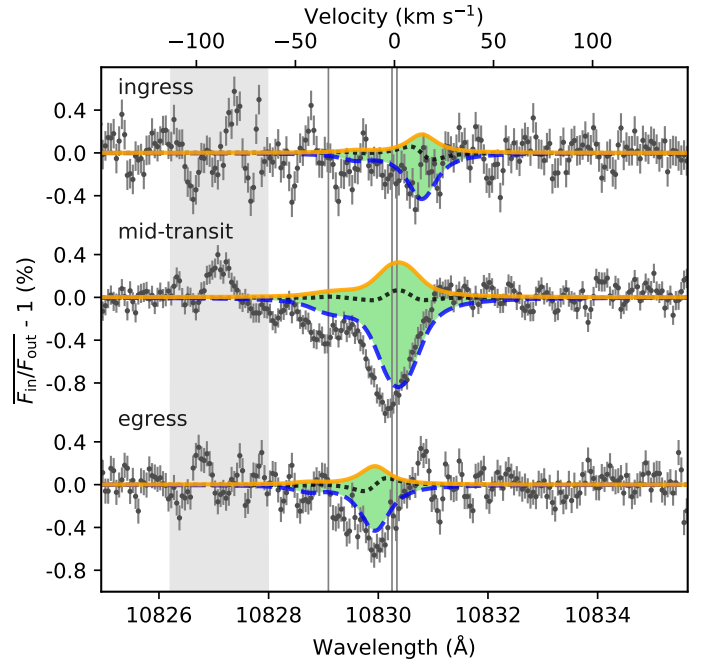
Fig. 6. Average stellar spectra around the He I λ10830 Å and He I λ5876 Å regions. The stellar spectra are shown by thick gray lines, models are depicted by thin blue lines, and integration regions for the equivalent widths are shaded.

Fig. 7. Pseudo-signals created by stellar surface heterogeneity shown in comparison to the observed ingress, mid-transit, and egress signals. The transit over dark patches creates pseudo-emission (orange solid lines), and a transit over bright patches creates a pseudo-absorption signal (blue dashed lines). Between the two extremes is the possible range of pseudo-signal contribution to the observed signal (green shaded areas). The gray dotted line indicates the impact of the RME neglecting stellar surface inhomogeneity.

model to calculate spectral time series with the planet occulting only He I dark or bright patches. The occulted spectrum was removed from the in-transit spectrum and division by the out-of-transit spectrum provided the model residual spectra, which were averaged for the ingress, mid-transit, and egress phases to obtain estimates for the pseudo-signals.

The resulting pseudo-signals are shown in Fig. 7. The pseudo-absorption signal is on a par in strength with the observed signal at all phases, but several features of the observations are not reproduced: (i) the model predicts too little absorption during mid-transit, 10.6 mÅ compared to the observed 12.7 ± 0.6 mÅ; (ii) the line ratio of the pseudo-absorption reflects that of the host star of 6.2, which is inconsistent with the observed value of 2.8 ± 0.2; (iii) the pseudo-absorption line is redshifted by 4.5 km s^{-1} with respect to the observations at mid-transit; (iv) the model predicts symmetric red- and blueshifted absorption at ingress and egress, which is not observed. Furthermore, such strong pseudo-absorption signals need a very special geometric configuration as the planet traverses about 10% of the stellar disk during the mid-transit phase and these signals would have to cover only bright stellar surface patches that also cover only 25% of the stellar disk. Moreover, this configuration would have to be very similar for all three transits, which were observed more than one year apart.

These shortcomings make it unlikely that the observed transit signals are exclusively pseudo-signals. However, the observed radial velocities of the absorption line during ingress and egress, place the planetary signal close to the stellar rest frame, which hinders a clear distinction between planetary absorption and stellar pseudo-signals. At any rate, an active star can produce strong features in the residual He I spectra with an amplitude anywhere between the limiting cases presented in Fig. 7.

A special case of the above assumptions that is very likely to interfere with the planetary signal are center-to-limb variations in the stellar He I λ10830 Å lines. The Sun shows limb-darkening in the He I λ10830 Å lines, i.e., the chromospheric He I absorption profile is deeper at the solar rim than in the center of the disk (de Jager et al. 1966). This modulation produces phase-dependent pseudo-signals. If the He I λ10830 Å lines of HD 189733 behave as those of much less active Sun, we would expect pseudo-emission signals during ingress and egress, and a pseudo-absorption signal during the mid-transit phase. Such a stellar contribution to the supposed planetary absorption signal would place the radial velocity of the absorption signal between the planetary and stellar rest frames during the mid-transit phase. This may have contributed to deflections from the planetary rest frame that are suggested in Fig. 2, but since they only affected the first two nights, where the instrumental stability was suboptimal, we refrain from further interpretations.

In this context, we also investigated the impact of the RME in the He I λ10830 Å lines. Assuming that the He I lines are homogeneous on the stellar disk, the RME causes signals with an amplitude of less than 0.07% in the residual spectra (see Fig. 7). The effect is negligible during the mid-transit phase and it is smaller than the possible impact of center-to-limb variations during the ingress and egress phases. Therefore, we do not include the RME in the following analysis.

4.2. Transmission spectrum modeling

We now assume the other extreme, namely a homogeneous stellar He I disk that causes no pseudo-signals. Neglecting the structure of the planetary atmosphere as well, we modeled the

Table 3. MCMC results with 1σ errors.

Phase	f^a (%)	$N_{\mathrm{He\,I}}^*$ (10^{11} cm^{-2})	b^b (km s^{-1})	Rad. vel. (km s^{-1})	Line ratio	χ_{red}^2 (174 DOF^c)	p-value
			extended atmosphere				
T_1–T_2	9.5	0.62 ± 0.11	15.0 ± 5.0	6.4 ± 3.2		1.15	0.09
T_2–T_3	20	1.04 ± 0.03	15.1 ± 0.6	-3.7 ± 0.4	7.9	1.34	0.002
T_3–T_4	9.5	1.07 ± 0.07	13.7 ± 1.0	-12.2 ± 0.9		1.17	0.06
			compact atmosphere				
T_1–T_2	0.58	12.9 ± 2.2	13.0 ± 4.9	6.6 ± 3.0		1.14	0.10
T_2–T_3	1.1	35.7 ± 2.0	11.3 ± 0.5	-3.3 ± 0.4	4.6	1.05	0.30
T_3–T_4	0.58	29.8 ± 3.7	11.7 ± 0.9	-13.0 ± 0.9		1.17	0.07

Notes. [a]Adopted covering fraction of the stellar disk covered by the planetary atmosphere. [b]Doppler parameter given by $\sqrt{2}$ times the velocity dispersion of the Gaussians. [c]DOF: degrees of freedom.

wavelength-dependent transmission, $T(\lambda)$, with a single absorption component:

$$T(\lambda) = (1 - f) + f \exp\left[-N_{\mathrm{He\,I}}^* \sigma(\lambda)\right]. \tag{1}$$

Here, f denotes the fraction of the stellar disk covered by the He I cloud, $N_{\mathrm{He\,I}}^*$ the column density of excited helium, and $\sigma(\lambda)$ the wavelength-dependent absorption cross section, which we parameterized by three Gaussians with their central wavelengths and oscillator strengths fixed to the known values from atomic physics (see National Institute of Standards and Technology, NIST; Drake 2006). The free parameters in our model are therefore the covering fraction, the He I column density in the triplet state, and a common velocity shift and line width.

Since the covering fraction and the column density are highly correlated, we adopted two opposing extreme values of $f = 1.1\%$ and 20% in our analysis. Assuming that the material is distributed in an annulus surrounding the opaque planet body, the covering fractions correspond to an atmosphere extending to 1.2 and 3.0 R_p[5]. The former represents the minimum atmospheric extent that can produce the observed 1% absorption signal and the latter is the effective Roche lobe radius of HD 189733 b (Eq. (2) of Eggleton 1983). In the following we refer to them as the compact and the extended assumption. For the ingress and egress phases, we derive the average covering fraction for an atmospheric ring at the exact observing times. To that end, we use analytic light curve models (Mandel & Agol 2002) and subtract the solid body light curve from that with an opaque atmosphere with the given expansion.

Adopting uniform priors for all parameters, we explored the posterior probability distributions with the Markov chain Monte Carlo technique[6] (MCMC). The chains were run over 10^5 steps with a burn-in of 10^4 steps. Our results for the ingress, mid-transit, and egress phase are summarized in Table 3. There we also provide χ^2 values and p-values for the null hypothesis that the maximum likelihood solution is true. Our maximum likelihood models are shown in Fig. 3.

From our spectral modeling, we find average radial velocities of 6.5 ± 3.1 km s^{-1} for ingress, -3.5 ± 0.4 km s^{-1} for mid-transit, and -12.6 ± 1.0 km s^{-1} for egress, independent of the adopted atmospheric extent. We stress once more that these velocities measurements are potentially affected by stellar pseudo-signals

(Sect. 4.1). At mid-transit, the ratio of the He I $\lambda 10830$ Å to $\lambda 10829$ Å components deviates from the optically thin ratio of 8 (NIST; Drake 2006). This can be explained by sufficiently large column densities, because saturation in the stronger component of the triplet increases the relative depth of the weaker component when the optically thin approximation breaks down. The observed ratio of 2.8 ± 0.2 corresponds to an optical depth of about 3.2 in the main component (de Jager et al. 1966). While the signal during the ingress and egress phases is equivalently reproduced using either assumptions (see Table 3), the compact case provides a superior approximation for the mid-transit phase. In particular, the extended assumption yields a larger than observed line ratio of 7.9 and a total equivalent width of 11.4 mÅ, whereas the compact assumption results in an equivalent width of 12.0 mÅ and a line ratio of 4.6, which better reproduces the observed He I $\lambda 10829$ Å absorption. Formally, this is reflected by a decrease from 1.34 to 1.05 in the reduced χ^2 statistics (see Table 3) and a p-value of 0.3 for the compact assumption, which provides no evidence against the null. Finally, we note that the line ratio is also not fully recovered under the compact assumption because the main component becomes too broad before the depth of the minor component is reproduced. Nevertheless, the mid-transit line ratio strongly favors a small covering fraction, which corresponds to a compact atmosphere.

While we do not fit a proper atmosphere model here, the derived He I triplet state column density is to be understood as an effective value, which can be compared to theoretical models. From the evaporation model of Oklopčić & Hirata (2018) for HD 209458 b, we derived a weighted mean absorption height of 1.6 R_p with a column of about 7.9×10^{11} cm^{-2}. We used $N_{\mathrm{He\,I}}^* R_\mathrm{p}$ as weights, which accounts for the increasing geometric weight of higher atmospheric layers. Although the model is for the HD 209458 system, the column density lies between the values derived for our compact and extended cases considered above, which shows that absorption in a planetary atmosphere is a viable origin of the observed signals. It is not unlikely that evaporation models like those of Oklopčić & Hirata (2018) can reproduce the mid-transit signal. Our finding that a compact atmosphere better reproduces the data than a compact atmosphere does not exclude that the atmosphere of HD 189733 b is evaporating, but could simply mean that the helium triplet state is not significantly populated in atmospheric layers above 0.2 R_p.

In the end, neither of our fits is fully satisfactory, particularly in the region of the weaker triplet component at $\lambda 10829$ Å. We attribute this to shortcomings of the adopted model. A more

---

[5] The atmosphere starts at 1 R_p and has a radial extent of 0.2 or 2.0 R_p.
[6] See the PyAstronomy wrapper for PyMC (https://github.com/pymc-devs/pymc).

comprehensive model should consider both pseudo-signals and dedicated atmospheric transmission models.

4.3. Velocity structure and ingress–egress asymmetry

The observed absorption is about twice as strong at egress as at the ingress phase, and it exhibits velocity shifts from the planetary rest frame at all phases. If HD 189733 b was tidally locked and its atmosphere rotated as a solid body, we would expect symmetric radial velocities of the signals at ingress and egress of ± 3.5 km s^{-1} if the absorption arises in atmospheric layers at a height of 0.2 $R_{\rm p}$. However, the observed shifts are asymmetric and significantly exceed this value at egress. We see two plausible hypotheses explaining the observed features, viz., atmospheric circulation in a dense helium atmosphere or an additional upper, low-density, and asymmetrically expanding atmosphere.

4.3.1. Atmospheric circulation

Hydrodynamic models of the irradiated atmospheres of synchronized hot Jupiters predict rather complex circulation patterns. For the specific case of HD 189733 b, the atmospheric circulation model by Showman et al. (2013), which covers a pressure range in the atmosphere from 2 to 200×10^{-6} bar, predicts the presence of a superrotating equatorial jet, where the bulk velocity increases with height in the atmosphere. Additionally, the model shows a general day-to-night side flow across the poles in high altitude layers, which is the main cause for the predicted net blueshift of around -3 km s^{-1} of molecular absorption signals in transmission spectra (see Fig. 12 of Showman et al. 2013).

Molecular absorption of CO and H_2O indicate such a net blueshift (-1.7 ± 1.2 km s^{-1} and $-1.6^{+3.2}_{-2.7}$ km s^{-1}, respectively; Brogi et al. 2016, 2018). These signals are sensitive to pressure levels between 0.1 and 10^{-6} bar. In contrast, ground-based high-resolution transmission spectroscopy in the sodium lines is sensitive to the lower pressure levels ($<10^{-6}$ bar) that are reached in the lower planetary thermosphere (Pino et al. 2018). Despite their origin in higher atmospheric layers, the sodium absorption signals of HD 189733 b indicate a net blueshift of -1.9 ± 0.7 km s^{-1} during mid-transit (Louden & Wheatley 2015). The helium absorption presented here likely probes even lower pressure levels in the planetary atmosphere. Particularly, the peak He I column density occurs at a pressure level of around 10^{-9} bar in the evaporation models of Oklopčić & Hirata (2018). Nevertheless, our mid-transit He I absorption signal also exhibits a significant blueshift of -3.5 ± 0.4 km s^{-1}, which is consistent with the previous results for the lower atmosphere.

At ingress and egress, the sodium signal indicates radial velocities of $+2.3^{+1.3}_{-1.5}$ km s^{-1} and $-5.3^{+1.0}_{-1.4}$ km s^{-1}, which are believed to be caused by an equatorial superrotating jet. At ingress the absorption signal is dominated by the leading limb where superrotating material moves away from the observer, which would explain the observed redshift. At egress the situation is reversed. The amplitude of the observed bulk velocities in the sodium signal are about a factor of 2.5 smaller than our results, but they do exhibit the same red- to blueshifted asymmetry (Louden & Wheatley 2015). While our He I ingress and egress velocities are also larger than those predicted by the circulation models of Showman et al. (2013), the observed pressure levels are clearly beyond the modeled atmospheric range.

If the advection timescale is comparable to the de-excitation timescale of the He I triplet state, the equatorial jet transports ground level helium atoms from the night side to the leading atmospheric limb and excited helium atoms from the dayside to the trailing limb. This naturally causes stronger He I λ10830 Å absorption at egress compared to the ingress phase. If we approximate the advection timescale by dividing the observed average ingress/egress radial velocities by the planetary radius, we derive a value of 10^{-4} s^{-1}. This is on the same order as the radiative transition rate to the ground level $A_{31} = 1.272 \times 10^{-4}$ s^{-1} (Drake 2006). Depending on the local conditions other processes could be faster in depopulating the metastable state, but it seems reasonable that the superrotating jet can also cause strong egress absorption through advection of excited helium atoms from the dayside.

Overall, the observations are consistent with previous observations and with the models of Showman et al. (2013) if the equatorial superrotating jet continues to exhibit increasing bulk velocities in higher atmospheric layers.

4.3.2. Asymmetric expanding atmosphere

The observed ingress signal is significant only at the 2σ level. If we attribute the redshift of the ingress signal to rednoise or another source unrelated to the planetary atmosphere, we are left with slightly blueshifted absorption at mid-transit and a larger blueshift at egress. The mid-transit signal is consistent with being caused by dense material in a compact atmosphere as shown in Sect. 4.2, but the density of the material that dominates the egress signal is not confined by our data.

The blueshifted radial velocities could be explained by material that evaporates from the planet and is subsequently being pushed backward, perhaps as a result of the stellar wind pressure creating an asymmetrically expanding atmosphere. The mechanism would be similar to the Type I interaction studied by Matsakos et al. (2015). In this case, the compact atmosphere that is observed during mid-transit causes only a small contribution to the observed egress signal similar to that during ingress. If the asymmetrically expanding atmosphere trails the planet, it would still cover the stellar disk at egress and dominate the observed absorption at this phase. The observed egress radial velocity would then be a measure of the bulk radial velocity of the evaporating material streaming away from the planet with velocity components pointing out of the system and in the reverse direction of orbit motion. At mid-transit the trailing material would be superposed onto that of the compact atmosphere causing the observed blueshift.

The nondetection of post-transit absorption constrains the (projected) extent of the hypothesized distribution of trailing material observed by means of He I in the triplet state. The lack of post-transit absorption could be explained by a tail structure that is nearly aligned with the star-planet axis. In fact, the 3D model of Spake et al. (2018) for WASP-107 b demonstrates that radiation pressure can create such a tail. However, we do not detect the strong blueshifts of the tail material predicted by the authors. A better explanation comes from the the spherical evaporation models of Oklopčić & Hirata (2018). The average absorption height for HD 209458 b was 1.6 $R_{\rm p}$ (Sect. 4.2), and the triplet state density quickly decreased at higher atmospheric levels. If this characteristic height also applies to an asymmetric extended atmosphere, it is consistent with our nondetection of post-transit absorption because excited helium atoms are not expected at large distances from the planet.

We therefore find the observations consistent with signals from a superposition of a dense, symmetric helium atmosphere and an asymmetrically expanding component that streams away from the planet and slightly trails it.

4.4. Comparison to Lyα absorption

Lyα observations have revealed variable absorption during the transit of HD 189733 b at high blueshifts between −230 and −140 km s^{-1} (Lecavelier des Etangs et al. 2012; Bourrier et al. 2013). Applying the same bootstrap method as in Sect. 3.4, we determine a mean absorption level of −0.017 ± 0.018% in this range, which is consistent with no He I absorption.

In the optically thin limit, the absorption EW is proportional to the cross section, σ, times the column density:

$$\text{EW} = N\sigma = \frac{N\lambda^2\pi e^2 f}{m_e c} \sim \lambda^2 f, \tag{2}$$

where λ is the central wavelength and f the oscillator strength. The two blended lines of the He I λ10830 Å triplet are by a factor of 90 more strongly absorbed than the hydrogen Lyα line (NIST; Drake 2006). The relative abundance of neutral hydrogen to that of helium in the metastable triplet state is about 10^5 in the simulations of Oklopčić & Hirata (2018). Thus, the Lyα line traces different atmospheric layers that can be a factor 10^3 more rarefied.

We note that Bourrier & Lecavelier des Etangs (2013) interpreted the Lyα absorption signal of HD 189733 b in terms of the presence of energetic neutrals created through charge exchange of stellar wind protons with neutrals in the planetary atmosphere. Energetic neutrals comprise a different population and their density depends on parameters like the stellar wind density and velocity. Currently, we cannot assess whether charge exchange can also create substantial amounts of helium in the excited triplet state. The variability of the Lyα signal, with absorption detected in only about half of the observations (Bourrier et al. 2013), is in contrast with the stability of the helium absorption signal. This fosters the picture that the two signals arise in populations that are decoupled to a larger degree, i.e., that the Lyα absorption at large blueshifts originates from the interaction of the stellar wind with the planetary atmosphere, and that the helium absorption occurs in the thermosphere closer to the planetary body.

5. Conclusions

We present the detection of spectrally resolved He I absorption signals in the near-infrared during three individual transit observations of HD 189733 b with CARMENES. The mid-transit signal in the He I λ10830 Å main component has a depth of 0.88 ± 0.04%. It exhibits a net blueshift of −3.5 ± 0.4 km s^{-1}, and shows no detectable variation in strength between the three transits. The ingress and egress signals show red- and blueshifts of +6.5 ± 3.1 km s^{-1} and −12.6 ± 1.0 km s^{-1}, respectively.

Our analysis reveals that pseudo-signals induced by the stellar surface structure in the He I λ10830 Å lines might interfere with the atmospheric signal of the planet, but do not reproduce all features of the data. We consider it unlikely that pseudo-signals can exclusively explain the transit signal. In the worst case, we estimate that they could account for up to 80% of the detected signal strength. Additionally, pseudo-signals might also affect the measured radial velocities at all phases.

When interpreted in terms of planetary atmospheric absorption, a compact atmosphere is favored with an extent of 0.2 planetary radii, which is easily contained within the planetary Roche lobe. This is consistent with the lack of both clear pre- or post-transit absorption and He I at radial velocities exceeding the planetary escape velocity. We discuss two hypotheses to explain

the observed radial velocity signature, namely, atmospheric circulation in the upper planetary atmosphere and an asymmetric extended atmosphere of evaporating material.

Atmospheric circulation with equatorial superrotation has been indicated in observations of lower atmospheric layers, which it is also predicted by models, and here we propose that it might persist throughout the higher layers responsible for the He I absorption. The superrotation hypothesis hinges on the signals and radial velocity shifts during the ingress and egress phases. While we consider the latter significant, the result for the ingress phase is more uncertain. If we attribute the observed redshift during ingress to an unrelated source, such as red-noise interference or unaccounted for stellar effects, the case for atmospheric superrotation wanes. In this case, the hypothesis of an asymmetrically evaporating atmosphere that accounts for the blueshifted egress signal becomes more attractive. Indeed, models of planetary evaporation predict such structures and Lyα observations have demonstrated the existence of material at large blueshifts exceeding −140 km s^{-1}. However, the lower radial velocity of the helium signal shows that we observe a different region of the planetary atmosphere.

Our analysis shows that transit spectroscopy of the He I line is a highly promising tool for the study of planetary atmospheric physics. Although, the atmosphere of HD 189733 b is almost certainly escaping from the planet, as evidenced by the Lyα observations, it remains uncertain how well the mass-loss rate can be determined from He I λ10830 Å absorption and to what degree the atmospheric absorption can be distinguished from stellar pseudo-signals. Detailed modeling is needed to investigate the physical plausibility of the two sketched interpretations, and only new observations will allow us to distinguish between them by a confirmation or rejection of the ingress signal.

References

Agol, E., Cowan, N. B., Knutson, H. A., et al. 2010, ApJ, 721, 1861
Allart, R., Lovis, C., Pino, L., et al. 2017, A&A, 606, A144

Andretta, V., Giampapa, M. S., Covino, E., Reiners, A., & Beeck, B. 2017, ApJ, 839, 97

Astropy Collaboration (Robitaille, T. P., et al.) 2013, A&A, 558, A33

Avrett, E. H., Fontenla, J. M., & Loeser, R. 1994, in Infrared Solar Physics, eds. D. M. Rabin, J. T. Jefferies, & C. Lindsey, IAU Symp., 154, 35

Baliunas, S. L., Donahue, R. A., Soon, W. H., et al. 1995, ApJ, 438, 269

Ballester, G. E., & Ben-Jaffel, L. 2015, ApJ, 804, 116

Baluev, R. V., Sokov, E. N., Shaidulin, V. S., et al. 2015, MNRAS, 450, 3101

Barnes, J. R., Haswell, C. A., Staab, D., & Anglada-Escudé, G. 2016, MNRAS, 462, 1012

Ben-Jaffel, L., & Ballester, G. E. 2013, A&A, 553, A52

Ben-Jaffel, L., & Sona Hosseini S. 2010, ApJ, 709, 1284

Birkby, J. L., de Kok, R. J., Brogi, M., et al. 2013, MNRAS, 436, L35

Bouchy, F., Udry, S., Mayor, M., et al. 2005, A&A, 444, L15

Bourrier, V., & Lecavelier des Etangs, A. 2013, A&A, 557, A124

Bourrier, V., Lecavelier des Etangs, A., Dupuy, H., et al. 2013, A&A, 551, A63

Boyajian, T., von Braun, K., Feiden, G. A., et al. 2015, MNRAS, 447, 846

Brogi, M., de Kok, R. J., Albrecht, S., et al. 2016, ApJ, 817, 106

Brogi, M., Giacobbe, P., Guilluy, G., et al. 2018, A&A, 615, A16

Brown, A. G. A., Vallenari, A., Prusti, T., et al. 2018, A&A, 616, A1

Caballero, J. A., Guàrdia, J., López del Fresno, M., et al. 2016, in Observatory Operations: Strategies, Processes, and Systems VI, Proc. SPIE, 9910, 99100E

Casasayas-Barris, N., Palle, E., Nowak, G., et al. 2017, A&A, 608, A135

Cauley, P. W., Redfield, S., & Jensen, A. G. 2017, AJ, 153, 217

Cegla, H. M., Lovis, C., Bourrier, V., et al. 2016, A&A, 588, A127

Claret, A., & Bloemen, S. 2011, A&A, 529, A75

Czesla, S., Klocová, T., Khalafinejad, S., Wolter, U., & Schmitt, J. H. M. M. 2015, A&A, 582, A51

de Jager, C., Namba, O., & Neven, L. 1966, Bull. Astron. Inst. Netherlands, 18, 128

de Kok, R. J., Brogi, M., Snellen, I. A. G., et al. 2013, A&A, 554, A82

Di Gloria, E., Snellen, I. A. G., & Albrecht, S. 2015, A&A, 580, A84

Drake, G. 2006, High Precision Calculations for Helium, ed. G. W. F. Drake, 199

Eggleton, P. P. 1983, ApJ, 268, 368

Ehrenreich, D., Lecavelier Des Etangs, A., Hébrard, G., et al. 2008, A&A, 483, 933

Ehrenreich, D., Bourrier, V., Wheatley, P. J., et al. 2015, Nature, 522, 459

Fossati, L., Haswell, C. A., Froning, C. S., et al. 2010, ApJ, 714, L222

Fulton, B. J., Petigura, E. A., Howard, A. W., et al. 2017, AJ, 154, 109

Gaia Collaboration (Prusti, T., et al.) 2016, A&A, 595, A1

Gibson, N. P., Aigrain, S., Pont, F., et al. 2012, MNRAS, 422, 753

Harvey, J. W., & Livingston, W. C. 1994, in Infrared Solar Physics, eds. D. M. Rabin, J. T. Jefferies, & C. Lindsey, IAU Symp., 154, 59

Haswell, C. A., Fossati, L., Ayres, T., et al. 2012, ApJ, 760, 79

Henry, G. W., & Winn, J. N. 2008, AJ, 135, 68

Huitson, C. M., Sing, D. K., Vidal-Madjar, A., et al. 2012, MNRAS, 422, 2477

Hünsch, M., Schmitt, J. H. M. M., Sterzik, M. F., & Voges, W. 1999, A&AS, 135, 319

Husser, T.-O., Wende-von Berg, S., Dreizler, S., et al. 2013, A&A, 553, A6

Indriolo, N., Hobbs, L. M., Hinkle, K. H., & McCall, B. J. 2009, ApJ, 703, 2131

Jensen, A. G., Redfield, S., Endl, M., et al. 2012, ApJ, 751, 86

Kausch, W., Noll, S., Smette, A., et al. 2015, A&A, 576, A78

Khalafinejad, S., von Essen, C., Hoeijmakers, H. J., et al. 2017, A&A, 598, A131

Klocová, T., Czesla, S., Khalafinejad, S., Wolter, U., & Schmitt, J. H. M. M. 2017, A&A, 607, A66

Knutson, H. A., Howard, A. W., & Isaacson, H. 2010, ApJ, 720, 1569

Kulow, J. R., France, K., Linsky, J., & Loyd, R. O. P. 2014, ApJ, 786, 132

Lammer, H., Selsis, F., Ribas, I., et al. 2003, ApJ, 598, L121

Lavie, B., Ehrenreich, D., Bourrier, V., et al. 2017, A&A, 605, L7

Lecavelier des Etangs, A., Vidal-Madjar, A., McConnell, J. C., & Hébrard, G. 2004, A&A, 418, L1

Lecavelier Des Etangs, A., Pont, F., Vidal-Madjar, A., & Sing, D. 2008, A&A, 481, L83

Lecavelier des Etangs, A., Ehrenreich, D., Vidal-Madjar, A., et al. 2010, A&A, 514, A72

Lecavelier des Etangs, A., Bourrier, V., Wheatley, P. J., et al. 2012, A&A, 543, L4

Linsky, J. L., Yang, H., France, K., et al. 2010, ApJ, 717, 1291

Louden, T., & Wheatley, P. J. 2015, ApJ, 814, L24

Lundkvist, M. S., Kjeldsen, H., Albrecht, S., et al. 2016, Nat. Commun., 7, 11201

Mandel, K., & Agol, E. 2002, ApJ, 580, L171

Matsakos, T., Uribe, A., & Königl, A. 2015, A&A, 578, A6

Mauas, P. J. D., Andretta, V., Falchi, A., et al. 2005, ApJ, 619, 604

McCullough, P. R., Crouzet, N., Deming, D., & Madhusudhan, N. 2014, ApJ, 791, 55

Moutou, C., Coustenis, A., Schneider, J., Queloz, D., & Mayor, M. 2003, A&A, 405, 341

Nortmann, L., Pallé, E., Salz, M., et al. 2018, Science, DOI:10.1126/science.aat5348

Ohta, Y., Taruya, A., & Suto, Y. 2005, ApJ, 622, 1118

Oklopčić, A., & Hirata, C. M. 2018, ApJ, 855, L11

Pillitteri, I., Wolk, S. J., Lopez-Santiago, J., et al. 2014, ApJ, 785, 145

Pino, L., Ehrenreich, D., Wyttenbach, A., et al. 2018, A&A, 612, A53

Piskunov, N. E., & Valenti, J. A. 2002, A&A, 385, 1095

Pont, F., Knutson, H., Gilliland, R. L., Moutou, C., & Charbonneau, D. 2008, MNRAS, 385, 109

Pont, F., Sing, D. K., Gibson, N. P., et al. 2013, MNRAS, 432, 2917

Poppenhaeger, K., Schmitt, J. H. M. M., & Wolk, S. J. 2013, ApJ, 773, 62

Quirrenbach, A., Amado, P. J., Caballero, J. A., et al. 2016, in Ground-based and Airborne Instrumentation for Astronomy VI, Proc. SPIE, 9908, 990812

Quirrenbach, A., Amado, P., Ribas, I., et al. 2018, Proc. SPIE, 10702

Redfield, S., Endl, M., Cochran, W. D., & Koesterke, L. 2008, ApJ, 673, L87

Rodler, F., Kürster, M., & Barnes, J. R. 2013, MNRAS, 432, 1980

Salz, M., Czesla, S., Schneider, P. C., & Schmitt, J. H. M. M. 2016, A&A, 586, A75

Sanz-Forcada, J., & Dupree, A. K. 2008, A&A, 488, 715

Sanz-Forcada, J., Micela, G., Ribas, I., et al. 2011, A&A, 532, A6

Schmitt, J. H. M. M., Fleming, T. A., & Giampapa, M. S. 1995, ApJ, 450, 392

Seager, S., & Sasselov, D. D. 2000, ApJ, 537, 916

Showman, A. P., Fortney, J. J., Lewis, N. K., & Shabram, M. 2013, ApJ, 762, 24

Sing, D. K., Désert, J.-M., Lecavelier Des Etangs, A., et al. 2009, A&A, 505, 891

Sing, D. K., Pont, F., Aigrain, S., et al. 2011, MNRAS, 416, 1443

Sing, D. K., Fortney, J. J., Nikolov, N., et al. 2016, Nature, 529, 59

Smette, A., Sana, H., Noll, S., et al. 2015, A&A, 576, A77

Spake, J. J., Sing, D. K., Evans, T. M., et al. 2018, Nature, 557, 68

Triaud, A. H. M. J., Queloz, D., Bouchy, F., et al. 2009, A&A, 506, 377

Vidal-Madjar, A., Lecavelier des Etangs, A., Désert, J.-M., et al. 2003, Nature, 422, 143

Vidal-Madjar, A., Désert, J.-M., Lecavelier des Etangs, A., et al. 2004, ApJ, 604, L69

Vidal-Madjar, A., Lecavelier des Etangs, A., Désert, J.-M., et al. 2008, ApJ, 676, L57

Vidal-Madjar, A., Huitson, C. M., Bourrier, V., et al. 2013, A&A, 560, A54

Watson, A. J., Donahue, T. M., & Walker, J. C. G. 1981, Icarus, 48, 150

Wyttenbach, A., Ehrenreich, D., Lovis, C., Udry, S., & Pepe, F. 2015, A&A, 577, A62

Yan, F., & Henning, T. 2018, Nat. Astron., 2, 714

Zarro, D. M., & Zirin, H. 1986, ApJ, 304, 365

Zechmeister, M., Reiners, A., Amado, P. J., et al. 2018, A&A, 609, A12

Appendix A: Complementary figures
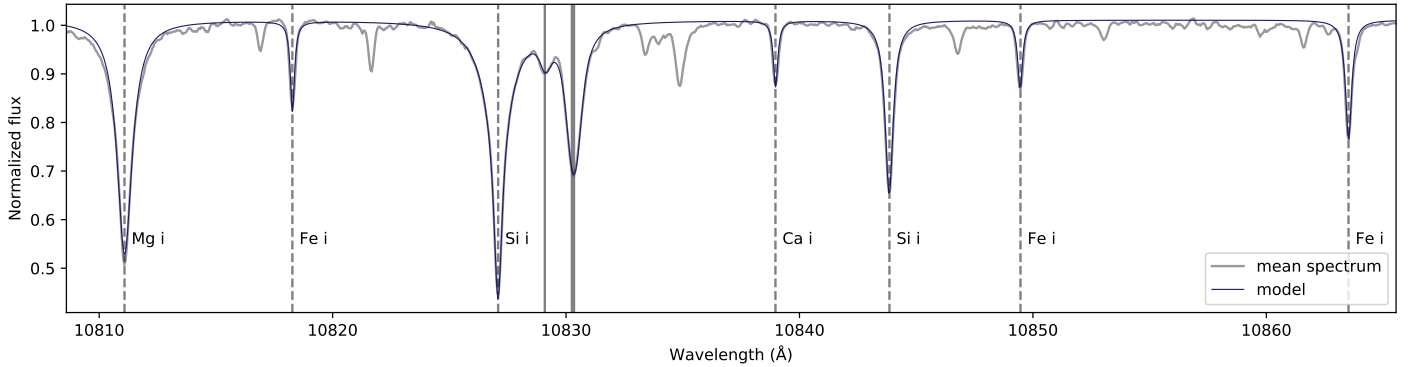
Fig. A.1. Spectral region of the He I λ10830 Å lines. The gray line is the average stellar spectrum, the dark-blue line is a model that includes the seven strongest stellar lines in the direct vicinity of the triplet lines used for the correction of the stellar rest frame. The position of the He I triplet is marked by vertical solid lines; the other seven spectral lines are labeled and marked by dashed lines.
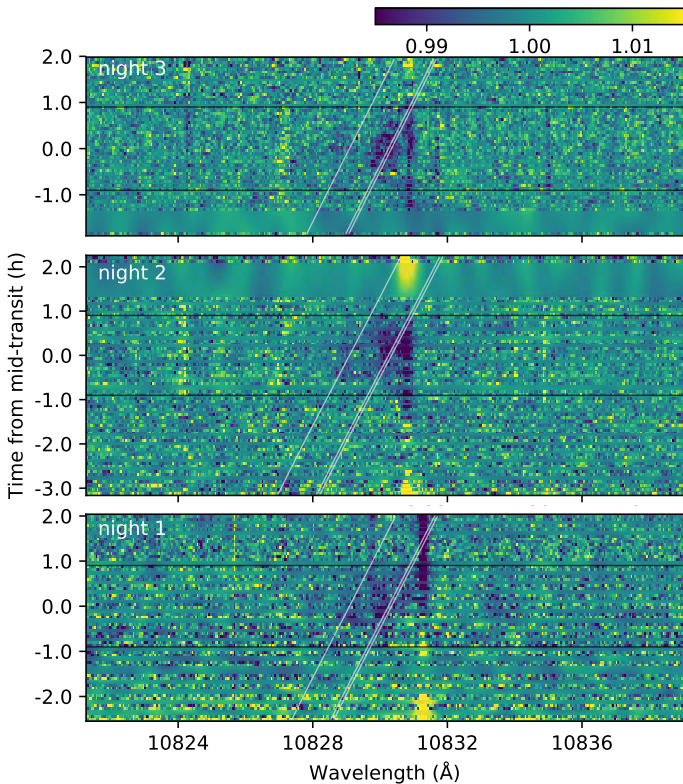

Fig. A.2. Residual spectra in the stellar rest frame before correction of the telluric emission lines (similar to Fig. 2).

Figure A.1 shows the stellar lines used to correct the alignment of all spectra in the stellar rest frame. Figure A.2 shows the residual spectra as depicted in Fig. 2, but without the removal of telluric emission lines. In the top panel of Fig. A.3, we display the average residual spectra during the mid-transit phase of the three individual transit observations. Finally, the bottom panel of Fig. A.3 depicts light curves centered on the minor component.
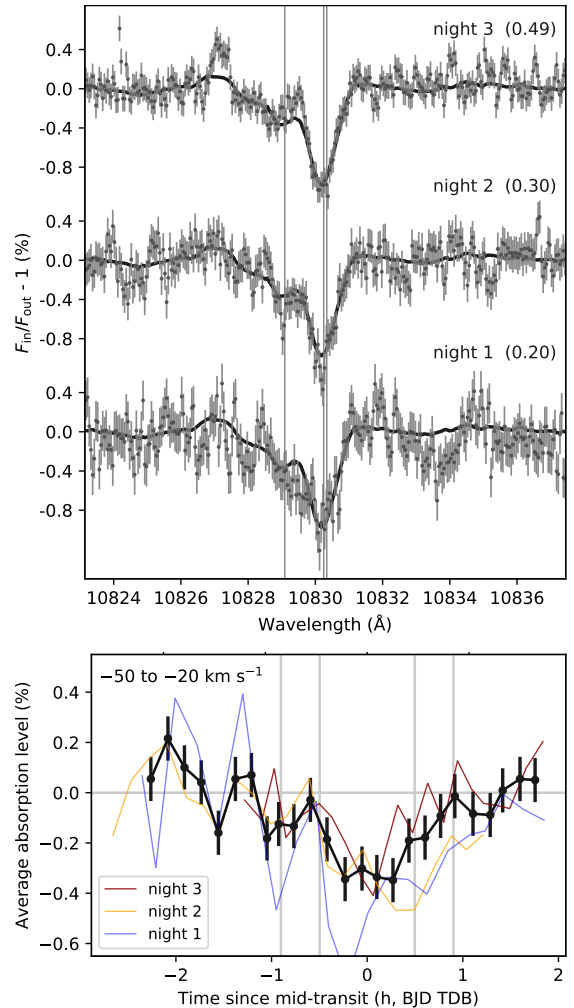
Fig. A.3. *Top panel:* transmission spectra of the three individual transits in the planetary rest frame. The He I triplet is indicated by vertical lines. In parentheses we provide the weights for computing the weighted mean absorption profile. For comparison, a smoothed version of the mean absorption profile is given by the black solid line. For a discussion, see Sects. 3.3 and 3.4. *Bottom panel:* same as Fig. 5, but for the He I λ10829 Å line.

Appendix B: Calcium IRT lines
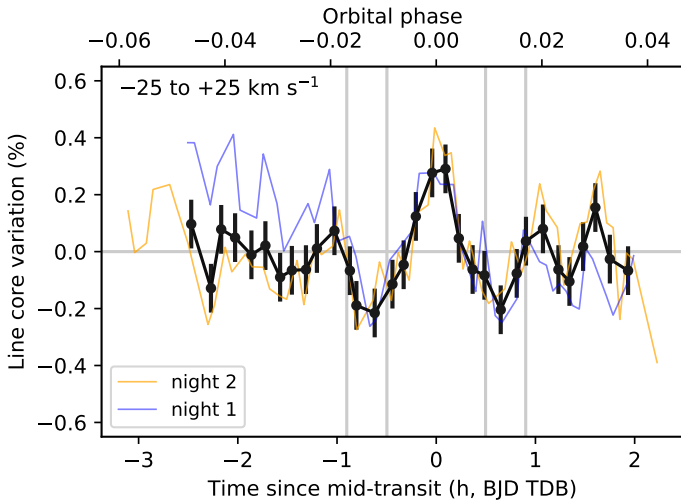
Fig. B.1. Light curves of the averaged three Ca IRT lines during the first two transit nights. The bold curve shows the mean light curve after correction of activity trends. Vertical lines mark the contact points of the optical transit.

To monitor the activity evolution of the host star, we checked the time evolution of the three Ca II IRT lines. We averaged the residual flux in a ± 25 km s^{-1} range in the line cores and then averaged the three individual lines. The resulting light curves are shown in Fig. B.1 for nights 1 and 2. The visual channel failed on night 3. Night 2 shows a slight activity trend that was fit linearly and subtracted before computing the mean IRT transit light curve. The light curve has the usual shape expected from center-to-limb variation in the stellar lines (Czesla et al. 2015). We find no indications of flaring activity, and in particular, we do not find evidence that the planet crossed unusually strong active regions during the two transit nights, which would cause larger excursions from the average light curve. This is consistent with our He I analysis.

Appendix C: Rossiter–McLaughlin effect

We derived relative radial velocity measurements for the NIR channel of CARMENES using SERVAL (Zechmeister et al. 2018). As described in Sect. 3.2, the instrument can exhibit nightly drifts with the configuration used. Therefore, we corrected linear trends from the radial velocity measurements. The resulting RVs are shown in Fig. C.1. The first two nights exhibit a large scatter. These observations were taken shortly after the instrument commissioning and the NIR spectrograph appears not to be fully stabilized yet (Quirrenbach et al. 2018).

We used only night 3 to fit the Rossiter–McLaughlin effect (RME) following the prescription of Ohta et al. (2005). The posterior distributions were explored with an MCMC chain of 10^5 steps with a burn-in of 10^4 steps. The reference mid-transit time, period, and semimajor axis were set-up with Gaussian priors according to the values in Table. 1. These parameters were not further confined by our data. The linear limb-darkening parameter was fixed to 0.43, which is the value calculated for the J band and a HD 189733-like star by Claret & Bloemen (2011). The
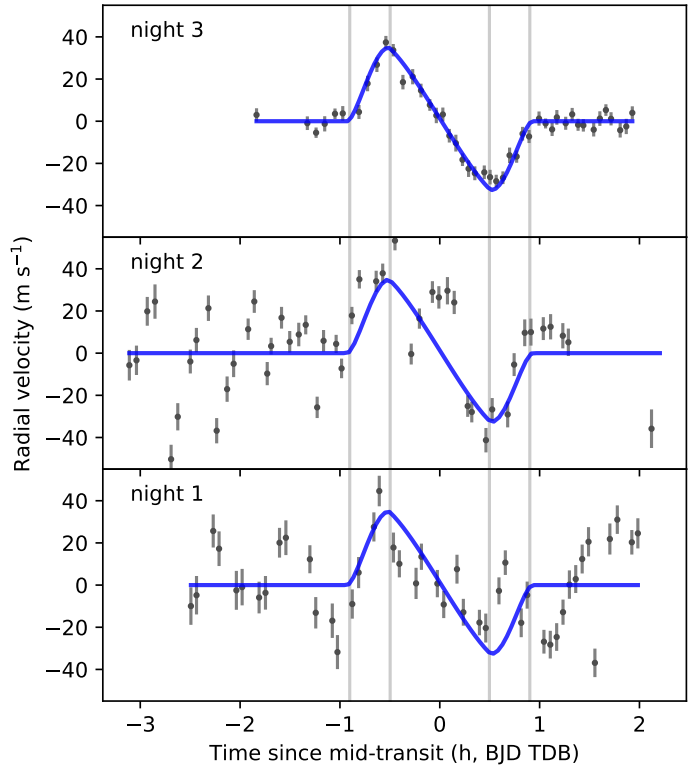
Fig. C.1. Radial velocity measurements of the NIR channel. A model of the RME is shown by the blue line. The four contact points are marked by vertical lines.

inclination of the stellar rotation axis was fixed to 92° (Cegla et al. 2016).

The remaining free parameters were the radius ratio, the rotation velocity of the host Ω, the inclination of the orbit i, and the obliquity λ. For the obliquity and the inclination, we find $\lambda = -1.6 \pm 1.1°$ and $i = 85.77 \pm 0.11°$, consistent with literature values (e.g., Triaud et al. 2009; Cegla et al. 2016; Casasayas-Barris et al. 2017). With a value of 0.162 ± 0.024, the radius ratio is only weakly confined by our data and consistent with all the literature values. For the angular rotation we find $\Omega = 0.40 \pm 0.11$ rad day^{-1}, which converts to a rotation period of 15.8 ± 4.6 days. This is somewhat larger than but still consistent with the well-determined value of 11.953 ± 0.009 (Henry & Winn 2008).

The slight discrepancy of the stellar rotation rate could be caused by differential rotation as noted by Cegla et al. (2016). Also, a wavelength dependence of the radius ratio (Di Gloria et al. 2015) would affect the measured stellar rotation rate. We further note that our RVs were determined with a cross-correlation technique, while the model assumed a line centroid method. A detailed analysis of the chromatic RME including the visual channel of CARMENES is beyond the scope of this paper.

Neither the stellar rotation period nor the radius ratio have any impact on our main conclusions here. The RME confirms the ephemeris used. The large scatter of the RVs during the first two observation nights shows that the instrument was less stable, and supports our analysis procedure to put the greatest weight on the observations during night 3.